



1 **OPTiMAL: A new machine learning approach for GDGT-based palaeothermometry**

2

3 Yvette L. Eley,¹ William Thomson², Sarah E. Greene¹, Ilya Mandel^{3,4}, Kirsty Edgar¹, James A. Bendle¹,
4 and Tom Dunkley Jones¹

5

6 **Affiliations:**

7 ¹School of Geography, Earth and Environmental Sciences, University of Birmingham, Edgbaston, B15
8 2TT, UK

9 ²School of Mathematics, University of Birmingham, Edgbaston, B15 2TT, UK

10 ³Institute of Gravitational Wave Astronomy, School of Physics and Astronomy, University of
11 Birmingham, Edgbaston, B15 2TT, UK

12 ⁴Monash Centre for Astrophysics, School of Physics and Astronomy, Monash University, Clayton,
13 Victoria 3800, Australia

14

15

16 **Abstract**

17

18 In the modern oceans, the relative abundances of Glycerol dialkyl glycerol tetraether (GDGTs) compounds
19 produced by marine archaeal communities show a significant dependence on the local sea surface
20 temperature at the site of formation. When preserved in ancient marine sediments, the measured abundances
21 of these fossil lipid biomarkers thus have the potential to provide a geological record of long-term variability
22 in planetary surface temperatures. Several empirical calibrations have been made between observed GDGT
23 relative abundances in late Holocene core top sediments and modern upper ocean temperatures. These
24 calibrations form the basis of the widely used TEX₈₆ palaeothermometer. There are, however, two
25 outstanding problems with this approach, first the appropriate assignment of uncertainty to estimates of
26 ancient sea surface temperatures based on the relationship of the ancient GDGT assemblage to the modern
27 calibration data set; and second, the problem of making temperature estimates beyond the range of the
28 modern empirical calibrations (>30 °C). Here we apply modern machine-learning tools, including Gaussian
29 Process Emulators and forward modelling, to develop a new mathematical approach we call OPTiMAL
30 (Optimised Palaeothermometry from Tetraethers via MACHine Learning) to improve temperature
31 estimation and the representation of uncertainty based on the relationship between ancient GDGT
32 assemblage data and the structure of the modern calibration data set. We reduce the root mean square
33 uncertainty on temperature predictions (validated using the modern data set) from $\sim\pm 6$ °C using TEX₈₆
34 based estimators to ± 3.6 °C using Gaussian Process estimators for temperatures below 30 °C. We also
35 provide a new but simple quantitative measure of the distance between an ancient GDGT assemblage and



36 the nearest neighbour within the modern calibration dataset, as a test for significant non-analogue
37 behaviour. Finally, we advocate against the use of temperature estimates beyond the range of the modern
38 empirical calibration dataset, given the absence – to date - of a robust predictive biological model or
39 extensive and reproducible mesocosm experimental data in this elevated temperature range.

40

41 **1. Introduction**

42

43 Glycerol dialkyl glycerol tetraethers (GDGTs) are membrane lipids consisting of isoprenoid carbon
44 skeletons ether-bound to glycerol (Schouten et al., 2013). In marine systems they are primarily produced
45 by ammonia oxidising marine Thaumarchaeota (Schouten et al., 2013), although some bacterial production
46 may also be important, especially in sub-freezing ecosystems (Siliakus et al., 2017). In modern marine core
47 top sediments, the relative abundance of GDGT compounds with more ring structures increases with the
48 mean annual sea surface temperature (SST) of the overlying waters (Schouten et al., 2002). This trend is
49 most likely driven by the need for increased cell membrane stability and rigidity at higher temperatures
50 (Sinninghe Damsté et al., 2002). On this basis, the TEX₈₆ (tetraether index of tetraethers containing 86
51 carbon atoms) ratio was derived to provide an index to represent the extent of cyclisation (Eq. 1; where
52 GDGT-x represents the fractional abundance of GDGT-x by LCMS peak area, and cren' is the peak area
53 of the regioisomer of crenarchaeol) (Schouten et al., 2002) and was shown to be positively correlated with
54 mean annual SSTs:

55

$$56 \text{TEX}_{86} = (\text{GDGT-2} + \text{GDGT-3} + \text{cren}') / (\text{GDGT-1} + \text{GDGT-2} + \text{GDGT-3} + \text{cren}') \quad (\text{Eq. 1})$$

57

58 Early applications of TEX₈₆ to reconstruct ancient SSTs were promising, especially in providing
59 temperature estimates in environments where standard carbonate-based proxies are hampered by poor
60 preservation (Schouten et al., 2003; Herfort et al., 2006; Schouten et al., 2007; Huguet et al., 2006; Sluijs
61 et al., 2006; Brinkhuis et al., 2006; Pearson et al., 2007; Sluijs et al., 2009). The TEX₈₆ approach also
62 extended beyond the range of the widely used alkenone-based U^k₃₇ thermometer, in both temperature space,
63 where U^k₃₇ saturates at ~28°C (Brassell, 2014; Zhaung et al., 2017), and back into the early Cenozoic (Bijl
64 et al., 2009; Hollis et al., 2009; Bijl et al., 2013; Inglis et al., 2015) and Mesozoic (Schouten et al., 2002;
65 Jenkyns et al., 2012; O'Brien et al., 2017) where haptophyte-derived alkenones are typically absent from
66 marine sediments (Brassell, 2014). Initially, TEX₈₆ was converted to SSTs using an equation derived by
67 Schouten et al. (2002) (Eq. 2):

68

$$69 \text{SST } ^\circ\text{C} = 66.7 * \text{TEX}_{86} - 18.7 \quad (\text{Eq. 2})$$



70

71 However as the number and range of applications of TEX_{86} palaeothermometry grew, concerns arose about
72 proxy behaviour at both the high (Liu et al., 2009) and low (Kim et al., 2008) temperature ends of the
73 modern calibration. In response to these criticisms, a new expanded modern core top dataset (Kim et al.,
74 2010) was used to generate two new forms of the GDGT proxy – TEX_{86}^L (Eq. 3), an exponential function
75 that does not include the crenarchaeol regio-isomer and was recommended for use across the entire
76 temperature range of the new core top data (-3 to 30 °C, particularly when SSTs are lower than 15 °C), and
77 TEX_{86}^H (Eq. 4), also exponential, and recommended for use when SSTs exceeded 15 °C (Kim et al. 2010).
78 TEX_{86}^L also excludes GDGT abundance data from the high-temperature regimes of the Red Sea, with the
79 rationale that high-salinity conditions are responsible for somewhat anomalous GDGT compositions in this
80 region (Kim et al. 2010).

81

$$82 \quad TEX_{86}^L = \log \left(\frac{[GDGT2]}{[GDGT1]+[GDGT2]+[GDGT3]} \right) \quad \text{Eq. 3}$$

83

84

$$85 \quad TEX_{86}^H = \log \left(\frac{[GDGT2]+[GDGT3]+[Cren']}{[GDGT1]+[GDGT2]+[GDGT3]+[Cren']} \right) \quad \text{Eq. 4}$$

86

87 Despite the recommendations of Kim et al. (2010), both TEX_{86}^H and TEX_{86}^L were widely used and tested
88 across a range of temperatures and palaeoenvironments, including comparisons against other
89 palaeotemperature proxy systems (Hertzberg et al., 2016; Zhang et al., 2014; Seki et al., 2014; Douglas et
90 al., 2014; Linnert et al., 2014; Tyler; Hollis et al. 2012; Dunkley Jones et al. 2013; Lunt 2012). The rationale
91 was that both TEX_{86}^L and TEX_{86}^H were calibrated across a full temperature range, with the exception of the
92 inclusion or exclusion of Red Sea core-top data. The difference in model fit between the two proxy
93 formulations to the calibration dataset was also minor (Kim et al. 2010). In certain environments, however,
94 TEX_{86}^L was subject to significant variability in derived temperatures that were not apparent in TEX_{86}^H
95 (Taylor et al. 2013). This was mostly due to changing GDGT2 to GDGT3 ratios, which strongly influence
96 TEX_{86}^L , and may be related to the GDGT productivity environment and deep-water lipid production, (Taylor
97 et al., 2013). As a result, TEX_{86}^L is no longer regarded as an appropriate tool for palaeotemperature
98 reconstructions, except in limited Polar conditions (Kim et al., 2010; Tierney, 2012).

99

100 Three fundamental issues have always troubled the TEX_{86} proxy. The first is a concern about undetected
101 non-analogue palaeo-GDGT assemblages, for which the modern calibration data set is inadequate to
102 provide a robust temperature estimation. Although various screening protocols, with independent indices



103 and thresholds, have been proposed to test for an excessive influence of terrestrial lipids (BIT index;
104 Hopmans et al. 2004), within sediment methanogenesis (Methane Index, 'MI'; Zhang et al., 2011) and non-
105 thermal effects such as nutrient levels and archaeal community structure to impact the weighted average of
106 cyclopentane moieties (Ring Index, 'RI'; Zhang et al., 2016), these do not provide a fundamental measure
107 of the proximity between GDGT abundance distributions in the modern, and ancient GDGT abundance
108 distributions recorded in sediment samples. The fundamental question remains – are measured ancient
109 assemblages of GDGT compounds anything like the modern assemblages, from which palaeotemperatures
110 are being estimated? Understanding this question is not helped by the use of indices – TEX₈₆ itself, or BIT
111 and MI – that collapse the dimensionality of GDGT abundance relationships onto a single axis of variation.
112

113 Second, from the earliest applications of the TEX₈₆ proxy to deep-time warm climate states (Schouten et
114 al., 2003) it was recognized that reconstructed temperatures beyond the range of the modern calibration
115 (>30 °C), were highly sensitive to model choice within the modern calibration range. Thus, Schouten et al.
116 (2003) restricted their calibration data for deep-time temperature estimates to core-top data in the modern
117 with mean annual SSTs over 20 °C. However, this problem of model choice, and its impact on temperature
118 estimation beyond the modern calibration range, persists (Hollis et al. in review), with current arguments
119 focused on whether there is an exponential (e.g. Cramwinckel et al., 2018) or linear (Tierney & Tingley,
120 2015) dependency of TEX₈₆ on SSTs, and the effect of these models on temperature estimates over 30 °C.
121

122 Culture and mesocosm studies are sometimes cited in support of extrapolations beyond the modern
123 calibration range when reconstructing ancient SSTs (Kim et al., 2010, Hollis et al., in review). However,
124 close examination of these culture studies reveals a significant variation in the patterns of archaeal GDGT
125 production in response to increasing growth temperature (e.g., Elling et al., 2015). At present, there are a
126 limited number of pure Thaumarchaeotal strains that can be cultured in the laboratory (Qin et al., 2014,
127 2015). Of the existing studies on these cultures, several focus on non-thermal environmental or
128 physiological variables, such as oxygen availability (Qin et al., 2015), that may also influence TEX₈₆. Early
129 mesocosm studies indicated that a TEX₈₆ to temperature relationship was maintained up to ~35-40 °C, but
130 with differing linear slopes from modern core top calibrations (Schouten et al., 2007; Wuchter et al., 2004).
131 The production of the crenarchaeol regional isomer (cren') in these elevated temperature mesocosms is
132 typically lower than that found in sediments (Pearson & Ingalls, 2013; Schouten et al., 2007), indicating
133 that the GDGT production environment in the mesocosms was in some fundamental way not analogous to
134 the time-averaged GDGT assemblages recovered from core-top samples. A more recent study of three pure
135 archaeal cultures (Elling et al. 2015) found that TEX₈₆ ratios for two of the three cultures showed positive
136 relationships with growth temperature (but with different slopes and intercepts), while the third, an isolate



137 from the surface waters of the South Atlantic, showed no relationship between TEX_{86} and growth
138 temperature. The available evidence is that there is not a uniform response in GDGT-production to growth
139 temperature across distinct strains of archaea in culture (Elling et al., 2015). More fundamentally, in natural
140 systems, it is likely that aggregated GDGT abundance variations in response to growth temperatures result
141 from changing compositions of archaeal populations as well as the physiological response of individual
142 strains to growth temperature (Elling et al. 2015). For instance, a multiproxy study of Mediterranean
143 Pliocene-Pleistocene sapropels indicates that specific distributions of archaeal lipids might be reflective of
144 temporal changes in thaumarchaeal communities rather than temperature alone (Polik et al., 2018). Indeed,
145 the potential influence of community switching on GDGT composition can be seen in mesocosm studies,
146 with different species preferentially thriving at different growth temperatures (e.g., Schouten et al., 2007).
147 To use the responses of single, selected archaeal strains in culture to validate a particular model of
148 community-level responses to growth temperature is clearly problematic even in the modern system (Elling
149 et al., 2015). For deep time applications it is even more difficult, where there is no independent constraint
150 on the archaeal strains dominating production or their evolution through time (Elling et al. 2015). What is
151 notable, however, is that the Ring Index (RI) - calculated using all commonly measured GDGTs (Zhang et
152 al., 2016) – has a more robust relationship with culture temperature between archaeal strains than TEX_{86} ,
153 indicating a potential loss of information within the TEX_{86} index (Elling et al. 2015).

154

155 Finally, traditional uses of the TEX_{86} proxy poorly represent the true uncertainty of palaeotemperature
156 estimates, as they include no assessment of non-analogue behavior relative to the modern core-top data.
157 Instead, uncertainty is typically based on the residuals on the modern calibration, with no reference to the
158 relationship between GDGT distributions of an ancient sample and the modern calibration data. An
159 improved Bayesian uncertainty model “BAYSPAR” is now in widespread use for SST estimation, which
160 uses sub-sampling approaches to improve temperature estimation and model uncertainty (Tierney and
161 Tingley, 2015). The Bayesian approach, however, still does not appropriately model uncertainty based on
162 the structure of fossil GDGT abundances relative to modern data, and is insensitive to detecting wildly non-
163 analogue behaviour in ancient GDGT distributions, as it still functions on one-dimensional TEX_{86} index
164 values.

165

166 All empirical calibrations of GDGT-based proxies assume that mean annual SST is the master control on
167 GDGT assemblages both today and in the past. Mean annual SST, however, is strongly correlated with
168 many other environmental variables (e.g., seasonality, pH, mixed layer depth, and productivity). In the
169 modern calibration dataset, mean annual SST shows the strongest correlation with TEX_{86} index (Schouten
170 et al., 2002), but this does not preclude an important (but undetectable) influence of these other



171 environmental variables. The use of empirical GDGT calibrations to infer ancient sea surface temperatures
172 thus implicitly assumes that the relationships between mean annual SST and all other GDGT-influencing
173 variables are invariant through time. This assumption is inescapable until, and unless, a more complete
174 biological mechanistic model of GDGT production emerges.

175

176 Here, we return to the primary modern core-top GDGT assemblage data (Tierney and Tingley, 2015), and
177 systematically explore the relationships between the modern GDGT distributions and surface ocean
178 temperatures using powerful mathematical tools. These tools can investigate correlations without prior
179 assumptions on the best form of relationship or *a priori* selection of GDGT compounds to be used. This
180 analysis is then extended through the exploration of the relationships between the modern core top GDGT
181 distributions and two compilations of ancient GDGT datasets, one from the Eocene (Inglis et al. 2015) and
182 one from the Cretaceous (O'Brien et al. 2017). We explore simple metrics to answer the fundamental
183 question – are modern core-top GDGT distributions good analogues for ancient distributions? We propose
184 the first robust methodology to answer this question, and so screen for significantly non-analogue palaeo-
185 assemblages. From this, we go on to derive a new machine learning approach 'OPTiMAL' (Optimised
186 Palaeothermometry from Tetraethers via MACHine Learning) for reconstructing SSTs from GDGT
187 datasets, which outperforms previous GDGT palaeothermometers and includes robust error estimates that,
188 for the first time, accounts for model uncertainty.

189

190 **2. Models for GDGT-based Temperature Reconstruction**

191

192 Our new analyses use the modern core-top data compilation, and satellite-derived estimates of SSTs, of
193 Tierney and Tingley (2015) as well as compilations of Eocene (Inglis et al. 2015) and Cretaceous (O'Brien
194 et al. 2017) GDGT assemblages. Within these fossil assemblages, only data points with full characterisation
195 of individual GDGT relative abundances were used. We also note that, in the first instance, all available
196 fossil assemblage data were interrogated, although later comparisons between BAYSPAR and our new
197 temperature predictor excludes fossil data that was regarded as unreliable based on standard pre-screening
198 indices, as noted within the original compilations (Inglis et al. 2015; O'Brien et al. 2017). All data used in
199 this study are tabulated in the supplementary information.

200

201 In order to enable meaningful comparison between new and existing temperature predictors, we use the
202 following consistent procedure for evaluating all predictors throughout this paper. We divide the modern
203 core-top data set of 854 data points into 85 validation data points (chosen randomly) and 769 calibration
204 points. We calibrate the predictor on the calibration points, and then judge its performance on the validation



205 points using the square root of the average of the square of the difference between the prediction at each
206 validation point, and the true (i.e. measured) temperature value:

207

$$\delta T = \sqrt{\frac{1}{N_v - 1} \sum_{k=1}^{N_v} (\hat{T}(x_k) - T(x_k))^2}$$

208

209 (Eq. 5)

210

211 where the sum is taken over each of $N_v = 85$ validation points, T is the known measured temperature (which
212 we refer to as the true temperature) and \hat{T} is the predicted temperature. For conciseness, we refer to δT as
213 the predictor standard error. It is useful to compare the accuracy of the predictor to the standard deviation
214 of all temperatures in the data set σT , which corresponds to using the mean temperature as the predictor in
215 Equation 1; for the modern data set, $\sigma T = 10.0$ °C. The so-called coefficient of determination R^2 , given by
216

$$R^2 \equiv 1 - \left(\frac{\delta T}{\sigma T}\right)^2$$

217

218 (Eq. 6)

219

220 provides a measure of the fraction of the fluctuation in the temperature explained by the predictor. To
221 facilitate performance comparisons between different methods of predicting temperature, we use the same
222 subset of validation points for all analyses. To avoid sensitivity to the choice of validation points, we repeat
223 the calibration-validation procedure for 10 random choices from the validation dataset.

224

225 2.1 Nearest neighbours

226

227 We begin with an agnostic approach to using some combination of the six observables - GDGT-0, GDGT-
228 1, GDGT-2, GDGT-3, crenarchaeol and the crenarchaeol regio-isomer (cren'), which we will jointly refer
229 to as GDGTs - to predict sea surface temperatures. Whatever functional form the predictor might take, it
230 can only provide accurate temperature predictions if nearby points in the six-dimensional observable space
231 - i.e. the distribution of all of the six commonly reported GDGTs - can be translated to nearby points in
232 temperature space. Conversely, if nearby points in the observable space correspond to vastly different
233 temperatures, then no predictor, regardless of which combination of GDGTs are used, will be able to
234 provide a useful temperature estimate. In other words, the structuring of GDGT distributions within multi-



235 dimensional space, must have some correspondence to the temperatures of formation (or rather the mean
236 annual SSTs used for standard calibrations).

237

238 We therefore consider the prediction offered by the temperature at the nearest point in the GDGT parameter
239 space. Of course, nearness depends on the choice of the distance metric. For example, it may be that sea
240 surface temperatures are very sensitive to one observable, so even a small change in that observable
241 corresponds to a significant distance, and rather insensitive to another, meaning that even with a large
242 difference in the nominal value of that observable the distance is insignificant. In the first instance, we use
243 a very simple Euclidian distance estimate $D_{x,y}$ where the distance along each observable is normalised by
244 the total spread in that observable across the entire data set. This normalisation ensures that a dimensionless
245 distance estimate can be produced even when observables have very different dynamical ranges, or even
246 different units. Thus, the normalised distance D between parameter data points x and y is

247

248

$$D_{x,y}^2 \equiv \sum_{i=0}^6 \frac{GDGT_i(x) - (GDGT_i(y))^2}{var(GDGT_i)}$$

249

(Eq. 7)

250

251 We show the distribution of nearest distances of points in the modern data set, excluding the sample itself,
252 in (Fig. 1).

253

254 The nearest-sample temperature predictor is $\hat{T}_{\text{nearest}}(x) = T(y)$ where y is the nearest point to x over the
255 calibration data set, i.e., one that minimises $D_{x,y}$. Fig. 2 shows the scatter in the predicted temperature when
256 using the temperature of the nearest data point to make the prediction. Overall, the failure of the nearest-
257 neighbour predictor to provide accurate temperature estimates even when the normalised distance to the
258 nearest point is small, $D_{x,y} \leq 0.5$, casts doubt on the possibility of designing an accurate predictor for
259 temperature based on GDGT observations. This is most likely due to additional environmental controls on
260 GDGT abundance distributions in natural systems, in particular the water depth (Zhang and Liu, 2018),
261 nutrient availability (Hurley et al., 2018; Polik et al., 2018; Park et al., 2018), seasonality, growth rate
262 (Elling et al., 2014) and ecosystem composition (Polik et al., 2018), that obscure a predominant relationship
263 to mean annual SSTs.

264

265 On the other hand, the standard error for the nearest-neighbour temperature predictor is $\delta T_{\text{nearest}} = 4.5$ °C.
266 This is less than half of the standard deviation σT in the temperature values across the modern data set.
267 Thus, the temperatures corresponding to nearby points in GDGT observable space also cluster in
268 temperature space. Consequently, there is hope that we can make some useful, if imperfect, temperature



269 predictions. The value of $\delta T_{\text{nearest}}$ will also serve as a useful benchmark in this design: while we may hope
270 to do better by, say, suitably averaging over multiple nearby calibration points rather than adopting the
271 temperature at one nearest point as a predictor, any method that performs worse than the nearest-neighbour
272 predictor is clearly suboptimal.

273

274 2.2 TEX_{86} and Bayesian applications

275

276 The TEX_{86} index reduces the six-dimensional observable GDGT space to a single number. While this has
277 the advantage of convenience for manipulation and the derivation of simple analytic formulae for
278 predictors, as illustrated below, this approach has one critical disadvantage: it wastes significant information
279 embedded in the hard-earned GDGT distribution data. Fig. 3 illustrates both the advantage and
280 disadvantage of TEX_{86} . On the one hand, there is a clear correlation between TEX_{86} and temperature (top
281 panel of Fig. 3), with a correlation coefficient of 0.81 corresponding to an overwhelming statistical
282 significance of 10^{-198} . On the other hand, very similar TEX_{86} values can correspond to very different
283 temperatures. We can apply the nearest-neighbour temperature prediction approach to the TEX_{86} value
284 alone rather than the full GDGT parameter space; this predictor yields a large standard error of $\delta T_{\text{nearestTEX}_{86}}$
285 = 8.0 °C (bottom panel of Fig. 3). While smaller than σT , this is significantly larger than $\delta T_{\text{nearest}}$ (Fig. 2),
286 consistent with the loss of information in TEX_{86} . We therefore do not expect other predictors based on
287 TEX_{86} to perform as well as those based on the full available data set.

288

289 Indeed, this is what we find when we consider predictors of the form $\hat{T}_{1/\text{TEX}} = a + b/\text{TEX}_{86}$ and $\hat{T}_{\text{TEXH}} = c$
290 + $d \log_{\text{TEX}_{86}}$ (Liu et al., 2009; Kim et al., 2010), i.e., the established relationships between GDGT
291 distributions and SST. We fit the free parameters a , b , c , and d by minimising the sum of squares of the
292 residuals over the calibration data sets. We find that $\delta T_{1/\text{TEX}} = 6.1$ °C (note that this is slightly better than
293 using the fixed values of a and b from (Kim et al., 2010), which yield $\delta T_{1/\text{TEX}} = 6.2$ °C). We note that the
294 corresponding R^2 value associated with these TEX_{86} based predictors is 0.64, which is lower than the R^2
295 values in Kim et al. (2010). We attribute this to the fact that we are using a larger dataset based on Tierney
296 and Tingley (2015), including data from the Red Sea (Kim et al. 2010).

297

298 Tierney and Tingley (2014) proposed a more sophisticated approach to obtaining the transfer function from
299 TEX_{86} to temperature, continuing to use simple linear regression, but with the addition of Gaussian
300 processes to model spatial variability in the temperature- TEX_{86} relationship and working with a forward
301 model which is subsequently inverted to produce temperature predictions. This forward model
302 ‘BAYSPAR’ is capable of generating an infinite number of calibration curves relating TEX_{86} to sea surface



303 temperatures (Tierney and Tingley, 2014). In order to derive a calibration for a specific dataset, the user
304 edits a range of parameters which vary depending on whether the dataset in question is from the relatively
305 recent past or deep time (Tierney and Tingley, 2014). For deep time applications, the authors propose a
306 modern analogue-type approach, in which they search the modern data for $20^\circ \times 20^\circ$ grid boxes containing
307 'nearby' TEX_{86} measurements and subsequently apply linear regression models calibrated on the analogous
308 samples for making predictions.

309

310 However, along with the simpler TEX_{86} -based models described above, this approach still suffers from the
311 arbitrary reduction of a six-dimensional data set to a single number. Therefore, it is not surprising that even
312 the simplest nearest-neighbour predictor (such as the one described above) that makes use of the full six-
313 dimensional dataset outperforms single-dimensional forward modelling approaches. Additionally,
314 uncertainty estimates do not account for the fact that TEX_{86} is, fundamentally, an empirical proxy, and so
315 its validity outside the range of the modern calibration is not guaranteed. This is a fundamental issue for
316 attempts to reconstruct surface temperatures during Greenhouse climate states, when tropical and sub-
317 tropical SSTs were likely hotter than those observed in the modern oceans.

318

319 *2.3 Machine learning Approaches – Random Forests*

320

321 There are a number of options to improve on nearest-neighbour predictions using machine learning
322 techniques such as artificial neural networks and random forests. These flexible, non-parametric models
323 would ideally be based on the underlying processes driving the GDGT response to temperature, but since
324 these processes remain unconstrained at present, we choose to deploy models which can reasonably reflect
325 predictive uncertainty and will be sufficiently adaptable in future (as new information regarding controls
326 on GDGTs emerge). These machine learning approaches are all based on the idea of training a predictor by
327 fitting a set of coefficients in a sufficiently complex multi-layer model in order to minimise residuals on
328 the calibration data set. As an example of the power of this approach, we train a random forest of decision
329 trees with 100 learning cycles using a least-squares boosting to fit the regression ensemble. Figure 4 shows
330 the prediction accuracy for this random forest implementation. This machine learning predictor yields δT
331 $= 4.1^\circ\text{C}$ degrees, outperforming the naive nearest-neighbour predictor by effectively applying a suitable
332 weighted average over multiple near neighbours. This corresponds to a very respectable $R^2 = 0.83$, meaning
333 that 83% of the variation in the observed temperature is successfully explained by our GDGT-based model.

334

335 *2.4 Gaussian Process Regression*

336



337 One downside of the random forest predictor is the difficulty of accurately estimating the uncertainty on
338 the prediction (Mentch and Hooker, 2016), although this is possible with, e.g., a bootstrapping approach
339 (Coulston et al., 2016). Fortunately, Gaussian process (GP) regression provides a robust alternative. For
340 full details on GP regression refer to Williams and Rasmussen (2006) and Rasmussen and Nickisch (2010).
341 Loosely, the objective here is to search among a large space of smoothly varying functions of GDGT
342 compositions for those functions which adequately describe temperature variability. This, essentially, is a
343 way of combining information from all calibration data points, not just the nearest neighbours, assigning
344 different weights to different calibration points depending on their utility in predicting the temperature at
345 the input of interest. The trained Gaussian process learns the best choice of weights to fit the data. Typically,
346 the GP will give greater weight to closer points, but, as we discuss below, it will learn the appropriate
347 distance metric on the multi-dimensional GDGT input space.

348

349 The weighting coefficients learned by the GP emulator represent a covariance matrix on the GDGT
350 parameter space. We can use this as a distance metric to provide meaningfully normalised distances
351 between points, removing the arbitrariness from the nearest neighbour distance ($D_{x,y}$) definition used
352 earlier. If the temperature is insensitive to a particular GDGT input coordinate (i.e., the value of that input
353 has a minimal effect on the temperature) then points within GDGT space that have large differences in
354 absolute input values in that coordinate are still near. We find that Cren has very limited predictive power,
355 and so points with large Cren differences are close in term of the normalised distance. Conversely, if the
356 temperature is sensitive to small changes in a particular GDGT variant, then points with relatively nearby
357 absolute input values in that coordinate are still distant. We find that most GDGT parameters other than
358 Cren are comparably useful in predicting temperature, with GDGT-0 and GDGT-3 marginally the most
359 informative.

360

361 We use a Gaussian process model with a squared exponential kernel with automatic relevance
362 determination (ARD) to allow for a separate length scale for each GDGT predictor. We fit the GP
363 parameters with an optimiser based on quasi-Newton approximation to the Hessian. Prediction accuracy is
364 shown in Figure 5, and we find that $\delta T = 3.72$ °C, which is a substantial improvement over the existing
365 indices, at least on the modern data. As mentioned, the GP framework provides a natural quantification of
366 predictive uncertainty, which includes uncertainty about the learned function. This is in contrast to, for
367 example, the TEX_{86} proxy, whereby the uncertainty associated with the selection of the particular functional
368 form used for predictions is ignored. While Tierney & Tingley (2014) also use Gaussian processes to model
369 uncertainty, they model spatial variability in the TEX_{86} -temperature relationship with a Gaussian process



370 prior. While this is a valuable approach to understand regional effects in the TEX₈₆-temperature
371 relationship, it does not deal with the 'non-analogue' situations we are concerned with in this paper.

372

373 *2.5 Data Structure*

374

375 The random forest (Section 2.3) and GPR approaches (Section 2.4) are agnostic about any underlying bio-
376 physical model that might impart the observed temperature-dependence on GDGT relative abundances
377 produced by archaea. They are essentially optimized interpolation tools for mapping correlations between
378 temperature and GDGT abundances within the range of the modern calibration data set; they can make no
379 sensible inference about the behavior of this relationship outside of the range of this training data. To move
380 from interpolation within, to extrapolation beyond, the modern calibration requires an understanding of,
381 and model for, the temperature-dependence of GDGT production. To explore these relationships and the
382 extent to which the ancient and modern data reside in a coherent relationship within GDGT space, we
383 employed two forms of dimensionality reduction to enable visualisation of the data in two or three
384 dimensions. The fundamental point is that if temperature is the dominant control, all of the data should lie
385 approximately on a one-dimensional curve in GDGT space, and the arclength along this curve should
386 correspond to temperature; we will revisit this point below.

387

388 We first employed a version of principal component analysis (PCA) tailored to compositional data
389 (Aitchison, 1982, 1983; Aitchison and Greenacre, 2002; Filzmoser et al., 2009a; Filzmoser et al., 2009b;
390 Filzmoser et al., 2012). Taking into account the compositional nature of the data is important because the
391 sum-to-one constraint induces correlations between variables which are not accounted for by classical PCA.
392 Furthermore, apparently nonlinear structure in Euclidean space often corresponds to linearity in the simplex
393 (i.e. the restricted space in which all elements sum to one) (Egozcue et al., 2003). Figure 6 shows the
394 modern, Eocene and Cretaceous data projected onto the first two principal components. Aside from the
395 obvious outlying cluster of Cretaceous data, characterised by GDGT-3 fractions above 0.6, the bulk of the
396 data occupy a two-dimensional point cloud with a small amount of curvature. The large majority of the
397 Cretaceous data has more positive PC1 values relative to the modern data.

398

399 We also explored the data using diffusion maps (Coifman et al., 2005; Haghverdi et al., 2015), a nonlinear
400 dimensionality reduction tool designed to extract the dominant modes of variability in the data. Such
401 diffusion maps have been successfully used to infer latent variables that can explain patterns of gene
402 expression. In the case of biological organisms, this latent variable is commonly developmental age (called
403 pseudo-time) (Haghverdi et al., 2016). In our case, the assumption would be that this latent variable



404 corresponds to temperature. Inspection of the eigenvalues of the diffusion map transition matrix suggests
405 that four diffusion components are adequate to represent the data; we plot the second, third and fourth of
406 these components in Figure 7 for the modern and ancient data. The separate clusters marked 'A' are the
407 outlying Cretaceous points with high GDGT-3 values. The bulk of the modern data lies on the branch
408 marked 'B', while the bulk of the Cretaceous data lies on the branch marked 'C'. Notably, the majority of
409 the modern points lying on branch C are from the Red Sea, which suggests that the Red Sea data is essential
410 for understanding ancient climates (particularly Cretaceous climates).

411

412 The relationship between the first diffusion component and TEX_{86} for all data is shown in Figure 8. There
413 is a clear correlation, despite the presence of some outlying Cretaceous points, some of which are not shown
414 because they lie so far outside the majority data range within this projection. This suggests that TEX_{86} is,
415 in one sense, a natural one-dimensional representation of the data. We also plot the first diffusion
416 component for the modern data as a function of temperature (Figure 9). We see a similar pattern emerging
417 to that displayed by TEX_{86} - there is little sensitivity to temperature below 15 °C, and between ~20 and 25
418 °C. An interesting avenue for future research might be to explore the temperature-GDGT system from a
419 dynamical systems perspective, i.e. use simple mechanistic mathematical models to explore the
420 temperature-dependence of steady-state GDGT distributions. It may be that such models suggest that only
421 a few steady-states exist, and that temperature is a bifurcation parameter, i.e. it controls the switch between
422 the steady states. Note also the downward slope in the residual pattern in Figure 4 between 0 and 15-17
423 degrees celsius, and again at higher temperatures. This pattern is consistent with predictions that are biased
424 towards the centre of each 'cluster', i.e. a system which is not very sensitive to temperature, but can
425 distinguish between high and low temperatures reasonably well. This observation also links to recent culture
426 studies (Elling et al., 2015) and Pliocene-Pleistocene sapropel data (Polik et al., 2018), which support the
427 existence of discrete populations with unique GDGT-temperature relationships and that temporal changes
428 in population over time can drive changes in TEX_{86} .

429

430 *2.6 Forward Modelling*

431

432 Based on the analysis of the combined modern and ancient data structure outlined above, there appears to
433 be some consistency to underlying trends in the overall variance of GDGT relative abundances. These
434 trends provide some hope that models of this variance, and its relationship to sea surface temperature, within
435 the modern dataset could be developed to predict ancient SSTs. TEX_{86} and BAYSPAR are such models,
436 but they are limited by, first, the reduction of six-dimensional GDGT space to a one-dimensional index;
437 and second, by an *ad hoc* model choice – linear, exponential – that does not account for uncertainty in



438 model fit to the modern calibration data, and the resultant uncertainty in the estimation of ancient SSTs
439 relating to model choice. To overcome these issues, we develop a forward model based on a multi-output
440 Gaussian Process (Alvarez et al., 2012), which models GDGT compositions as functions of temperature,
441 accounting for correlations between GDGT measurements. This model is then inverted to obtain
442 temperatures which are compatible with a measured GDGT composition. In simple terms, we posit that a
443 measured GDGT composition is generated by some unknown function of temperature and corrupted by
444 noise, which may be due to measurement error or some unmodelled particularity of the environment in
445 which the sample was generated. We proceed by defining a large (in this case infinite) set of functions of
446 temperature to explore and compare them to the available data, throwing away those functions which do
447 not adequately fit the data. This means, of course, that the behaviour of the functions we accept is allowed
448 to vary more widely outside the range of the modern data than within it. With no mechanistic underpinning,
449 choosing only one function (such as the inverse of TEX_{86}) based on how well it fits the modern data grossly
450 underestimates our uncertainty about temperature where no modern analogue is available.

451

452 The forward modelling approach is similar to that of Haslett et al. (2006), who argue that it is preferable to
453 model measured compositions as functions of climate, before probabilistically inverting the model to infer
454 plausible climates given a composition. The cost of modelling the data in this more natural way is the loss
455 of degrees of freedom -- we are now attempting to fit a one-dimensional line through a multidimensional
456 point cloud rather than fit a multidimensional surface to the GDGT data, which means that the predictive
457 power of the model suffers, at least on the modern data. The existing BAYSPAR calibration also specifies
458 the model in the forward direction, but ignores model uncertainty. As with all GP models, the choice of
459 kernel has a substantial impact on predictions (and their associated uncertainty) outside the range of the
460 modern data, where predictions revert to the prior implied by the kernel. Given that we have no mechanistic
461 model for the data generating process, we recommend the use of kernels which do not impose strong prior
462 assumptions on the form of the GDGT-temperature relationship (e.g. kernels with a linear component) and
463 thus reasonably represent model uncertainty outside the range of the modern data. We choose a zero-mean
464 Matern 3/2 kernel for the applications below. Note, however, that since we are working in *ilr*-transformed
465 coordinates, this corresponds to a prior assumption of uniform compositions at all temperatures, i.e. all
466 components are equally abundant.

467

468 The residuals for the forward model are shown in Figure 10. The clear pattern in the residuals does not
469 necessarily indicate model misspecification, since no explicit noise model is specified for temperatures.
470 Predictive distributions are to be interpreted in the Bayesian sense, in that they represent a 'degree of belief'
471 in temperatures given the model and the modern data. The residual pattern is similar to that of the random



472 forest (Figure 4) with two clear downward slopes, suggesting again that the data are clustered into
473 temperatures above and below 16-17 degrees celsius, and that predictions tend towards temperatures at the
474 centres of these clusters.

475

476 An advantage of the forward modelling approach is that the inversion can incorporate substantive prior
477 information about temperatures for individual data points. In particular, other proxy systems can be used to
478 elicit prior distributions over temperatures to constrain GDGT-based predictions, particularly when
479 attempting to reconstruct ancient climates with no modern analogue in GDGT-space. We emphasise that
480 outside the range of the modern data, the utility of the models is almost solely due to the prior information
481 included in the reconstruction. At present, the only priors being used in the forward model prescribe a
482 reasonable upper limit and lower limit on temperatures (see Supplementary Information). The only way to
483 improve these reconstructions will be for future iterations to incorporate prior information from other
484 proxies. It is worth noting that the predictive uncertainty, while reasonably well-described by the standard
485 deviation in cases where ancient data lie quite close to the modern data in GDGT space, can be highly
486 multimodal (Fig. 11). This is the case when estimates are significantly outside of the modern calibration
487 dataset, such as low latitude data in the Cretaceous, or where there is considerable scatter in the modern
488 calibration data, for example in the low temperature range (<5 °C).

489

490 **3. Non-analogue behavior and Extrapolation**

491

492 In principle, the predictors described above can be applied directly to ancient data, such as data from the
493 Eocene or Cretaceous (Inglis et al., 2015; O'Brien et al., 2017). In practice, one should be careful with
494 using models outside their domain of applicability. The machine learning tools described above, which are
495 ultimately based on the analysis of nearby calibration data in GDGT space, are fundamentally designed for
496 *interpolation*. To the extent that ancient data occupy a very different region in GDGT space, *extrapolation*
497 is required, which the models do not adequately account for. The divergence between modern calibration
498 data and ancient data is evident from Fig. 12, which shows histograms of minimum normalised distances
499 between 'high quality' Eocene/Cretaceous data points (those that passed the screening tests applied by
500 O'Brien et al., 2017 and Inglis et al., 2015) and the nearest point in the full modern data set. We strongly
501 recommend the use of the nearest neighbor distance metric (D_{nearest}) as a screening method to determine
502 whether the modern core top GDGT assemblage data is an appropriate basis for ancient SST estimation on
503 a case-by-case basis. Note that this distance measure is weighted by the scale length of the relevant
504 parameter as estimated by the Gaussian process emulator in order to quantify the relative position of ancient
505 GDGT assemblages to the modern core-top data. By using the GP-estimated covariance as the distance



506 metric, we account for the sensitivity of different GDGT components to temperature. Our inference is that
507 samples with $D_{\text{nearest}} > 0.5$, *regardless of the calibration model or approach applied*, are unlikely to generate
508 temperature estimates that are much better than informed guesswork. In these instances, in both our GPR
509 and Fwd models, the constraints provided by the modern calibration data set are so weak that estimates of
510 temperature have large uncertainty bands that are dictated by model priors; i.e. are unconstrained by the
511 calibration data (e.g., Figure 13 and Figure 14). This uncertainty is not apparent from estimates generated
512 by BAYSPAR or TEX_{86}^H models, although the underlying and fundamental lack of constraints are the same.
513 While 93% of validation data points in the modern data have $D_{\text{nearest}} < 0.5$, this is the case for only 33% of
514 Eocene samples and 3% for Cretaceous samples.

515
516 Where ancient GDGT distributions lie far from the modern calibration data set ($D_{\text{nearest}} > 0.5$), we argue that
517 there is no suitable set of modern analogue GDGT distributions from which to infer growth temperatures
518 for this ancient GDGT distribution. Both the GPR and Fwd models revert to imposed priors once the
519 distance from the modern calibration dataset increases. We propose that this is more rigorous and justified
520 model behavior than extrapolation of TEX_{86} or BAYSPAR predictors to non-analogue samples far from
521 the modern calibration data. As a result, the predictive models can only be applied to a subset of the Eocene
522 and Cretaceous data. We also note that there are two broad, non-mutually-exclusive categories of samples
523 that lie far from the modern calibration dataset ($D_{\text{nearest}} > 0.5$), the first are samples that seem to lie ‘beyond’
524 the temperature-GDGT calibration relationship, likely with (unconstrained) GDGT formation temperatures
525 higher than the modern core-top calibrations; the second are samples with anomalous GDGT distributions
526 lying on the margins of, or far away from the main GDGT clustering in 6-dimensional space (see outliers
527 in Fig. 8).

528
529 Given the (current) limit on natural mean annual surface ocean temperatures of ~ 30 °C, extending the
530 GDGT-temperature calibration might be possible through, 1) integration of full GDGT abundance
531 distributions produced in high temperature culture, mesocosm or artificially warmed sea surface conditions
532 into the models; followed by, 2) validation through robust inter-comparisons of any new GDGT
533 palaeothermometer for high temperatures conditions with other temperature proxies from past warm
534 climate states. As discussed in the introduction, the first approach is limited by the ability of culture or
535 mesocosm experiments to accurately represent the true diversity and growth environments and dynamics
536 of natural microbial populations. Such studies clearly indicate a more complex, community-scale control
537 on changing GDGT relative abundances to growth temperatures (e.g., Elling et al., 2015). Community-
538 scale temperature dependency can be modelled relatively well with analyses of natural production preserved
539 in core-top sediments, especially with more sophisticated model fitting, including the GPR and Fwd model



540 presented here. Above $\sim 30^{\circ}\text{C}$, however, the behavior of even single strains of archaea are not well-
541 constrained by culture experiments, and the natural community-level responses above this temperature are,
542 so far, completely unknown. Significantly more culture and mesocosm data at these high temperatures,
543 spanning a range of microbial diversity and growth conditions, could provide some of these constraints in
544 future. Until such data exist, we see no robust justification for any particular extrapolation of modern core-
545 top calibration data sets into the unknown above 30°C , although the coherent patterns apparent across
546 GDGT space, between modern, Eocene and Cretaceous data (Figures 7), does provide some grounds for
547 hope that the extension of GDGT palaeothermometry beyond 30°C might be possible in future.

548

549 **4. OPTiMAL and D_{nearest} : A more robust method for GDGT-based paleothermometry**

550

551 A more robust framework for GDGT-based palaeothermometry, could be achieved with a flexible
552 predictive model that uses the full range of six GDGT relative abundances, and has transparent and robust
553 estimates of the prediction uncertainty. In this context, the Gaussian Process Regression model (GPR;
554 Section 2.4) outperforms the Forward model (Fwd; Section 2.6) within the modern calibration dataset and
555 we recommend standard use of the GPR model, henceforth called OPTiMAL, over the Fwd model. Model
556 code for the calculation of D_{nearest} values and OPTiMAL SST estimates (Matlab script) and the Fwd Model
557 SST estimates (R script) are archived in the GITHUB repository,
558 <https://github.com/carbonatefan/OPTiMAL>.

559

560 To investigate the behaviour of the new OPTiMAL model, we compare temperature predictions including
561 uncertainties for the Eocene and Cretaceous datasets, made by OPTiMAL and the BAYSPAR
562 methodology of Tierney and Tingley (2014) (Figures 13 and 14). The OPTiMAL model systematically
563 estimates slightly cooler temperatures than BAYSPAR, with the biggest offsets below $\sim 15^{\circ}\text{C}$ (Figure 13).
564 Fossil GDGT assemblages that fail the D_{nearest} test are shown in grey, which clearly illustrate the regression
565 to the mean in the OPTiMAL model, whereas BAYSPAR continues to make SST predictions up to and
566 exceeding 40°C for these “non-analogue” samples. A comparison of error estimation between OPTiMAL
567 and BAYSPAR is shown in Figure 14. For most of the predictive range below the D_{nearest} cut-off of 0.5,
568 OPTiMAL has smaller errors than BAYSPAR, especially in the lower temperature range. As D_{nearest}
569 increases, i.e. as the fossil GDGT assemblage moves further from the constraints of the modern calibration
570 dataset, the error on OPTiMAL increases, until it reaches the standard deviation of the modern calibration
571 dataset (i.e., is completely unconstrained). In other words, OPTiMAL generates maximum likelihood SSTs
572 with robust confidence intervals, which appropriately reflect the relative position of an ancient sample used
573 for SST estimation and the structure of the modern calibration data set. Where there are strong constraints



574 from near analogues in the modern data, uncertainties will be small, where there are weak constraints,
575 uncertainty increases. In contrast, BAYSPAR, because it is fundamentally based on a *parametric* linear
576 model and therefore does not account for model uncertainty, assigns similar uncertainty intervals as to the
577 rest of the data, despite there being no way of reasonably testing whether the linear model is an appropriate
578 description of the data far from the modern dataset.

579

580 **5. Conclusions**

581

582 Although the fundamental issue of non-analogue behaviour is a key problem for GDGT-temperature
583 estimation, it has an undue impact on the community's general confidence in this method. In part, this is
584 because these issues have not been clearly stated and circumscribed - rather they have been allowed to erode
585 confidence in the entire GDGT-based methodology through the inappropriate use of GDGT-based
586 palaeothermometry far outside the modern constraints on the behavior of this system. The use of GDGT
587 abundances to estimate temperatures in clearly non-analogue conditions is, at present, difficult to justify on
588 the basis of the available calibration constraints or a good understanding of underlying biophysical models.
589 We hope that this study prompts further investigations that will improve these constraints for the use of
590 GDGTs in deep-time paleoclimate studies, where they clearly have substantial potential as temperature
591 proxies. Temperature estimates based on fossil GDGT assemblages that are within range of, or similar to,
592 modern GDGT calibration data, do, however, rest on a strong, underlying temperature-dependence
593 observed in the empirical data. The failure to have an effective means of separating the "good from the bad",
594 either leads to false confidence and inappropriate inferences in non-analogue conditions, or a false
595 pessimism when the community's trust in the overall method is eroded by the clear influence of
596 methodological choice on SST estimates outside of the modern calibration range.

597

598 In this study, we apply modern machine-learning tools, including Gaussian Process Emulators and forward
599 modelling, to improve temperature estimation and the representation of uncertainty in GDGT-based SST
600 reconstructions. Using our new nearest neighbour test, we demonstrate that >60% of Eocene, and >90% of
601 Cretaceous, fossil GDGT distribution patterns differ so significantly from modern that it is inappropriate to
602 interpret them using modern empirical calibrations of any formulation. For data that does show sufficient
603 similarity to modern, we present OPTiMAL, a new multi-dimensional Gaussian Process Regression tool
604 which uses all six GDGTs (GDGT-0, -1, -2, -3, Cren and Cren') to generate an SST estimate with associated
605 uncertainty. The key advantages of the OPTiMAL approach are: 1) that these uncertainty estimates are
606 intrinsically linked to the strength of the relationship between the fossil GDGT distributions and the modern
607 calibration data set, and 2) by considering all GDGT compounds in a multi-dimensional regression model



608 it avoids the dimensionality reduction and loss of information that takes place when calibrating single
609 parameters (TEX_{86}) to temperature. The methods presented above make very few assumptions about the
610 data. We argue that such methods are appropriate with the current absence of any reasonable mechanistic
611 model for the data generating process, in that they reflect model uncertainty in a natural way.

612

613

614 **Acknowledgements:**

615 TDJ, JAB, IM, KME and YE acknowledge NERC grant NE/P013112/1. SEG was supported by NERC
616 Independent Research Fellowship NE/L011050/1 and NERC large grant NE/P01903X/1. WT
617 acknowledges the Wellcome Trust (grant code: 1516ISSFFEL9, www.wellcome.ac.uk/) for funding a
618 parameterisation workshop at the University of Birmingham (UK). WT, TDJ and IM would like to thank
619 the BBSRC UK Multi-Scale Biology Network Grant No. BB/M025888/1.

620

621

622

623 **Figure Captions:**

624

625

626 **Figure 1.** A histogram of the normalised distance to the nearest neighbour in GDGT space ($D_{x,yt}$) for all
627 samples in the modern calibration dataset of Tierney and Tingley (2015).

628

629 **Figure 2.** The error of the nearest-neighbour temperature ($D_{x,y}$) predictor, for modern core-top data, as a
630 function of the distance to the nearest calibration sample.

631

632 **Figure 3.** Top: The temperature of the modern data set as a function of the TEX_{86} value, showing a clear
633 correlation between the two, but also significant scatter. Bottom: the error of the predictor based on the
634 nearest TEX_{86} calibration point.

635

636 **Figure 4.** The error of a random forest predictor as a function of the true temperature.

637

638 **Figure 5.** The error of the GPR (Gaussian Process regression) predictor as a function of the true
639 temperature.

640

641 **Figure 6.** Modern and ancient data projected onto the first two compositional principal components. Black:
642 Modern; Blue: Eocene (Inglis et al., 2015); Red: Cretaceous (O'Brien et al., 2017).



643

644 **Figure 7.** Diffusion map projection of the modern and ancient data. Black: Modern; Blue: Eocene (Inglis
645 et al., 2015); Red: Cretaceous (O'Brien et al., 2017). separate clusters marked 'A' are the outlying
646 Cretaceous points with high GDGT-3 values. Branch 'B' is dominated by modern data points; branch 'C'
647 by Cretaceous data.

648

649 **Figure 8.** The first diffusion component as a function of TEX_{86} . Some outlying points have been excluded
650 from the plot for the purposes of visualisation. Black: Modern; Blue: Eocene (Inglis et al., 2015); Red:
651 Cretaceous (O'Brien et al., 2017).

652

653 **Figure 9.** The first diffusion component as a function of temperature (modern data only).

654

655 **Figure 10.** Temperature residuals for the forward model.

656

657 **Figure 11.** The posterior distributions over temperature from the forward model for selected examples of
658 high and low temperature, Eocene and Cretaceous, data points. The Gaussian error envelope from the GPR
659 model is shown for comparison.

660

661 **Figure 12.** A histogram of normalised distances to the nearest sample in the modern data set for Eocene
662 and Cretaceous data, excluding samples that had been screened out in previous compilations using BIT, MI
663 and RI following the approach of (Inglis et al., 2015; O'Brien et al., 2017).

664

665 **Figure 13.** Comparison of temperature estimates for the BAYSPAR and the OPTiMAL GPR model, greyed
666 out data fails the $D_{nearest}$ test (>0.5), and the colour scaling reflects $D_{nearest}$ values for those datapoints that
667 pass

668

669 **Figure 14.** Inter-comparison of temperature estimates (top) and errors (bottom) for the Eocene and
670 Cretaceous data calculated using BAYSPAR and OPTiMAL. Greyed out data fails the $D_{nearest}$ test (>0.5),
671 and the colour scaling reflects $D_{nearest}$ values for those datapoints that pass. The black dashed line shows the
672 $D_{nearest}$ threshold (>0.5).

673

674

675

676



677

678 **References:**

- 679 Aitchison, J.: The Statistical Analysis of Compositional Data. *J. R. Stat. Soc. Series B Stat. Methodol.* 44,
680 139–160, 1982.
- 681 Aitchison, J.: Principal component analysis of compositional data. *Biometrika* 70, 57–65, 1983.
- 682 Aitchison, J., Greenacre, M.: Biplots of compositional data. *J. R. Stat. Soc. Ser. C Appl. Stat.* 51, 375–392,
683 2002.
- 684 Álvarez, M.A., Rosasco, L., Lawrence, N.D.: Kernels for Vector-Valued Functions: A Review.
685 *Foundations and Trends® in Machine Learning* 4, 195–266, 2012.
- 686 Bijl, P. K., S. Schouten, A. Sluijs, G.-J. Reichert, J. C. Zachos, and H. Brinkhuis.: Early Palaeogene
687 temperature evolution of the southwest Pacific Ocean. *Nature*, 461, 776–779, 2009.
- 688 Bijl, P. K., Bendle, J.A.P., Bohaty, S.M., Pross, J., Schouten, S., Tauxe, L., Stickley, C., McKay, R.M.,
689 Röhl, U., Olney, M., Sluijs, A., Escutia, C., Brinkhuis, H. and Expedition 318 Scientists.: Eocene
690 cooling linked to early flow across the Tasmanian Gateway. *Proc. Natl. Acad. Sci. U.S.A.*, 110,
691 9645–9650, 2013.
- 692 Brassell, S. C.: Climatic influences on the Paleogene evolution of alkenones, *Paleoceanography*, 29, 255-
693 272, doi:10.1002/2013PA002576, 2014.
- 694 Brinkhuis, H., Schouten, S., Collinson, M. E., Sluijs, A., Damsté, J. S. S., Dickens, G. R., Huber, M.,
695 Cronin, T. M., Onodera, J., Takahashi, K., Bujak, J. P., Stein, R., van der Burgh, J., Eldrett, J. S.,
696 Harding, I. C., Lotter, A. F., Sangiorgi, F., Cittert, H. v. K.-v., de Leeuw, J. W., Matthiessen, J.,
697 Backman, J., Moran, K., and the Expedition, Scientists.: Episodic fresh surface waters in the
698 Eocene Arctic Ocean, *Nature*, 441, 606 – 609, 2006.
- 699 Coifman, R.R., Lafon, S., Lee, A.B., Maggioni, M., Nadler, B., Warner, F., Zucker, S.W.: Geometric
700 diffusions as a tool for harmonic analysis and structure definition of data: diffusion maps. *Proc.*
701 *Natl. Acad. Sci. U. S. A.* 102, 7426–7431, 2005.
- 702 Coulston, J.W., Blinn, C.E., Thomas, V.A.: Approximating prediction uncertainty for random forest
703 regression models. *Photogrammetric Engineering & Remote Sensing*, Volume 82, 189-197,
704 <https://doi.org/10.14358/PERS.82.3.189>, 2016.
- 705 Cramwinckel, M. J., Huber, M., Kocken, I. J., Agnini, C., Bijl, P. K., Bohaty, S. M., Frieling, J., Goldner,
706 A., Hilgen, F. J., Kip, E. L., Peterse, F., van der Ploeg, R., Röhl, U., Schouten, S., and Sluijs, A.:
707 Synchronous tropical and polar temperature evolution in the Eocene, *Nature*, 559, 382-386, 2018.
- 708 Douglas, P. M. J., Affek, H. P., Ivany, L. C., Houben, A. J. P., Sijp, W. P., Sluijs, A., Schouten, S., Pagani,
709 M.: Pronounced zonal heterogeneity in Eocene southern high-latitude sea surface temperatures.
710 *Proceedings of the National Academy of Sciences*, 111, 6582–6587, 2014.
- 711 Dunkley Jones, T., Lunt, D. J., Schmidt, D. N., Ridgwell, A., Sluijs, A., Valdes, P. J., and Maslin, M.:
712 Climate model and proxy data constraints on ocean warming across the Paleocene–Eocene Thermal
713 Maximum, *Earth-Science Reviews*, 125, 123-145, 2013.



- 714 Egozcue, J.J., Pawłowsky-Glahn, V., Mateu-Figueras, G., Barceló-Vidal, C.: Isometric Logratio
715 Transformations for Compositional Data Analysis. *Math. Geol.* 35, 279–300, 2003.
- 716 Elling, F. J., Könneke, M., Lipp, J. S., Becker, K. W., Gagen, E. J., and Hinrichs, K.-U.: Effects of growth
717 phase on the membrane lipid composition of the thaumarchaeon *Nitrosopumilus maritimus* and
718 their implications for archaeal lipid 20 distributions in the marine environment, *Geochimica et*
719 *Cosmochimica Acta*, 141, 579-597, 2014.
- 720 Elling, F. J., Könneke, M., Mußmann, M., Greve, A., and Hinrichs, K.-U.: Influence of temperature, pH,
721 and salinity on membrane lipid composition and TEX₈₆ of marine planktonic thaumarchaeal
722 isolates, *Geochimica et Cosmochimica Acta*, 171, 238-255, 2015.
- 723 Filzmoser, P., Hron, K., Reimann, C.: Principal component analysis for compositional data with outliers.
724 *Environmetrics* 20, 621–632, 2009a.
- 725 Filzmoser, P., Hron, K., Reimann, C., Garrett, R.: Robust factor analysis for compositional data. *Comput.*
726 *Geosci.* 35, 1854–1861, 2009b.
- 727 Filzmoser, P., Hron, K., Reimann, C.: Interpretation of multivariate outliers for compositional data.
728 *Comput. Geosci.* 39, 77–85, 2012.
- 729 Haghverdi, L., Buettner, F., Theis, F.J.: Diffusion maps for high-dimensional single-cell analysis of
730 differentiation data. *Bioinformatics* 31, 2989–2998, 2015.
- 731 Haghverdi, L., Büttner, M., Wolf, F.A., Buettner, F., Theis, F.J.: Diffusion pseudotime robustly
732 reconstructs lineage branching. *Nat. Methods* 13, 845–848, 2016.
- 733 Haslett, J., Whitley, M., Bhattacharya, S., Salter-Townshend, M., Wilson, S.P., Allen, J.R.M., Huntley, B.,
734 Mitchell, F.J.G.: Bayesian palaeoclimate reconstruction. *J Royal Statistical Soc A* 169, 395–438;
735 2006.
- 736 Herfort, L., Schouten, S., Boon, J. P., and Sinninghe Damsté, J. S.: Application of the TEX₈₆ temperature
737 proxy to the southern North Sea, *Organic Geochemistry*, 37, 1715-1726, 2006.
- 738 Hertzberg, J. E., Schmidt, M. W., Bianchi, T. S., Smith, R. K., Shields, M. R., & Marcantonio, F.:
739 Comparison of eastern tropical Pacific TEX₈₆ and Globigerinoides ruber Mg/Ca derived sea surface
740 temperatures: Insights from the Holocene and Last Glacial Maximum. *Earth and Planetary Science*
741 *Letters*, 434, 320–332, 2016.
- 742 Hollis, C. J., Taylor, K. W. R., Handley, L., Pancost, R. D., Huber, M., Creech, J. B., Hines, B. R., Crouch,
743 E. M., Morgans, 25 H. E. G., Crampton, J. S., Gibbs, S., Pearson, P. N., and Zachos, J. C.: Early
744 Paleogene temperature history of the Southwest Pacific Ocean: Reconciling proxies and models,
745 *Earth and Planetary Science Letters*, 349–350, 53-66, 2012.
- 746 Hollis, C. J., Dunkley Jones, T., Anagnostou, E., Bijl, P. K., Cramwinckel, M. J., Cui, Y., Dickens, G. R.,
747 Edgar, K. M., Eley, Y., Evans, D., Foster, G. L., Frieling, J., Inglis, G. N., Kennedy, E. M.,
748 Kozdon, R., Lauretano, V., Lear, C. H., Littler, K., Meckler, N., Naafs, B. D. A., Pälike, H.,
749 Pancost, R. D., Pearson, P., Royer, D. L., Salzmann, U., Schubert, B., Seebeck, H., Sluijs, A.,
750 Speijer, R., Stassen, P., Tierney, J., Tripathi, A., Wade, B., Westerhold, T., Witkowski, C., Zachos,
751 J. C., Zhang, Y. G., Huber, M., and Lunt, D. J.: The DeepMIP contribution to PMIP4:
752 methodologies for selection, compilation and analysis of latest Paleocene and early Eocene climate



- 753 proxy data, incorporating version 0.1 of the DeepMIP database, *Geosci. Model Dev. Discuss.*,
754 <https://doi.org/10.5194/gmd-2018-309>, in review, 2019.
- 755 Hollis, C. J., Handley, L., Crouch, E. M., Morgans, H. E., Baker, J. A., Creech, J., Collins, K. S., Gibbs, S.
756 J., Huber, M., Schouten, S.: Tropical sea temperatures in the high-latitude South Pacific during the
757 Eocene. *Geology*, 37, 99–102, 2009.
- 758 Hopmans, E. C., Weijers, J. W. H., Schefuss, E., Herfort, L., Sinninghe Damsté, J. S., Schouten, S.: A
759 novel proxy for terrestrial organic matter in sediments based on branched and isoprenoid tetraether
760 lipids, *Earth and Planetary Science Letters*, 224, 107–116, 2004.
- 761 Huguet C, Kim J-H, Sinninghe Damsté J.S., Schouten S: Reconstruction of sea surface temperature
762 variations in the Arabian Sea over the last 23 kyr using organic proxies (TEX₈₆ and UK 0 37 .
763 *Paleoceanography* 21(3): PA3003, 2006.
- 764 Hurley, S. J., Elling, F. J., Könneke, M., Buchwald, C., Wankel, S. D., Santoro, A. E., Lipp, J.S., Hinrichs,
765 K., Pearson, A.: Influence of ammonia oxidation rate on thaumarchaeal lipid composition and the
766 TEX₈₆ temperature proxy. *Proceedings of the National Academy of Sciences*, 113, 7762–7767,
767 2016.
- 768 Inglis, G. N., Farnsworth, A., Lunt, D., Foster, G. L., Hollis, C. J., Pagani, M., Jardine, P. E., Pearson, P.
769 N., Markwick, P., Galsworthy, A. M. J., Raynham, L., Taylor, K. W. R., and Pancost, R. D.:
770 Descent toward the Icehouse: Eocene sea surface cooling inferred from GDGT distributions,
771 *Paleoceanography*, 30, 1000–1020, 2015.
- 772 Jenkyns H.C., Schouten-Huibers L., Schouten S., Damsté J.S.S.: Warm Middle Jurassic–Early Cretaceous
773 high-latitude sea-surface temperatures from the Southern Ocean. *Clim Past* 8 (1):215–226, 2012.
- 774 Kim, J.-H., Schouten, S., Hopmans, E. C., Donner, B., and Sinninghe Damsté, J. S.: Global sediment core-
775 top calibration of the TEX₈₆ paleothermometer in the ocean, *Geochimica et Cosmochimica Acta*,
776 72, 1154–1173, 2008.
- 777 Kim, J.-H., van der Meer, J., Schouten, S., Helmke, P., Willmott, V., Sangiorgi, F., Koç, N., Hopmans, E.
778 C., and Sinninghe Damsté, J. S.: New indices and calibrations derived from the distribution of
779 crenarchaeal isoprenoid tetraether lipids: Implications for past sea surface temperature
780 reconstructions, *Geochimica et Cosmochimica Acta*, 74, 4639–4654, 2010.
- 781 Linnert, C., Robinson, S. A., Lees, J. A., Bown, P. R., Perez-Rodriguez, I., Petrizzo, M. R., Falzoni, F.,
782 Littler, K., Antonio Arz, J., Russell, E. E. : Evidence for global cooling in the Late Cretaceous.
783 *Nature Communications*, 5, 1–7, 2014.
- 784 Lunt, D. J., Dunkley Jones, T., Heinemann, M., Huber, M., LeGrande, A., Winguth, A., Loptson, C.,
785 Marotzke, J., Tindall, J., Valdes, P., Winguth, C.: A model-data comparison for a multi-model
786 ensemble of early Eocene atmosphere-ocean simulations: EoMIP, *Clim. Past Discuss.*, 8, 1229-
787 1273, 2012.
- 788 Mentch, L., Hooker, G.: Quantifying Uncertainty in Random Forests via Confidence Intervals and
789 Hypothesis Tests. *Journal of Machine Learning Research*, 17, 1–41, 2016.
- 790 O'Brien, C. L., Robinson, S. A., Pancost, R. D., Sinninghe Damsté, J. S., Schouten, S., Lunt, D. J., Alsenz,
791 H., Bornemann, 20 A., Bottini, C., Brassell, S. C., Farnsworth, A., Forster, A., Huber, B. T., Inglis,



- 792 G. N., Jenkyns, H. C., Linnert, C., Littler, K., Markwick, P., McAnena, A., Mutterlose, J., Naafs, B.
793 D. A., Püttmann, W., Sluijs, A., van Helmond, N. A. G. M., Vellekoop, J., Wagner, T., Wrobel, N.
794 E.: Cretaceous sea-surface temperature evolution: Constraints from TEX₈₆ and planktonic
795 foraminiferal oxygen isotopes, *Earth-Science Reviews*, 172, 224-247, 2017.
- 796 Park, E., Hefter, J., Fischer, G., Mollenhauer, G.: TEX₈₆ in sinking particles in three eastern Atlantic
797 upwelling regimes. *Organic Geochemistry*, 124, 151–163, 2018.
- 798 Pearson, P. N., van Dongen, B. E., Nicholas, C. J., Pancost, R. D., Schouten, S., Singano, J. M., Wade, B.
799 S.: Stable warm tropical climate through the Eocene Epoch. *Geology*, 35, 211-214, 2007.
- 800 Polik, C. A., Elling, F. J., Pearson, A.: Impacts of Paleoecology on the TEX₈₆ Sea Surface Temperature
801 Proxy in the Pliocene-Pleistocene Mediterranean Sea. *Paleoceanography and Paleoclimatology*, 33,
802 1472–1489, 2018.
- 803 Qin, W., Amin, S. A., Martens-Habbena, W., Walker, C. B., Urakawa, H., Devol, A. H., Ingalls, A.E.,
804 Moffett, J.W., Ambrust, E.V., Stahl, D. A.: Marine ammonia-oxidizing archaeal isolates display
805 obligate mixotrophy and wide ecotypic variation. *Proceedings of the National Academy of*
806 *Sciences of the United States of America*, 111, 12504–12509, 2014.
- 807 Qin, W., Carlson, L. T., Ambrust, E. V., Stahl, D. A., Devol, A. H., Moffett, J. W., Ingalls, A. E.:
808 Confounding effects of oxygen and temperature on the TEX 86 signature of marine
809 Thaumarchaeota. *Proceedings of the National Academy of Sciences*, 112, 10979–10984, 2015.
- 810 Rasmussen, C.E., Nickisch, H.: Gaussian Processes for Machine Learning (GPML) Toolbox. *J. Mach.*
811 *Learn. Res.* 11, 3011–3015, 2010.
- 812 Sangiorgi, F., van Soelen Els, E., Spofforth David, J. A., Pälike, H., Stickley Catherine, E., St. John, K.,
813 Koç, N., Schouten, S., Sinninghe Damsté Jaap, S., Brinkhuis, H.: Cyclicity in the middle Eocene
814 central Arctic Ocean sediment record: Orbital forcing and environmental response,
815 *Paleoceanography*, 23, 10.1029/2007PA001487, 2008.
- 816 Schouten, E., Hopmans, E.C., Forster, A., Van Breugel, Y., Kuypers, M.M.M., Sinninghe Damsté, J.S.:
817 Extremely high seasurface temperatures at low latitudes during the middle Cretaceous as revealed
818 by archaeal membrane lipids. *Geology*, 31, 1069–1072, 2003.
- 819 Schouten, S., Forster, A., Panoto, F. E., and Sinninghe Damsté, J. S.: Towards calibration of the TEX₈₆
820 palaeothermometer for 20 tropical sea surface temperatures in ancient greenhouse worlds, *Organic*
821 *Geochemistry*, 38, 1537-1546, 2007.
- 822 Schouten, S., Hopmans, E. C., Sinninghe Damsté, J. S.: The organic geochemistry of glycerol dialkyl
823 glycerol tetraether lipids: A review, *Organic Geochemistry*, 54, 19-61, 2013.
- 824 Schouten, S., Hopmans, E. C., Schefuß, E., Sinninghe Damsté, J. S.: Distributional variations in marine
825 crenarchaeotal membrane lipids: a new tool for reconstructing ancient sea water temperatures?
826 *Earth and Planetary Science Letters*, 204, 15 265-274, 2002.
- 827 Seki, O., Bendle, J. A., Harada, N., Kobayashi, M., Sawada, K., Moossen, H., Sakamoto, T.: Assessment
828 and calibration of TEX₈₆ paleothermometry in the Sea of Okhotsk and sub-polar North Pacific
829 region: Implications for paleoceanography. *Progress in Oceanography*, 126, 254–266, 2014.



- 830 Siliakus, M., van der Oost, J., Kengen, S.W.M.: Adaptations of archaeal and bacterial membranes to
831 variations in temperature, pH and pressure. *Extremophiles*, 21, 651 – 670, 2017.
- 832 Sluijs A, Schouten S, Pagani M, Woltering, M., Brinkhuis, H., Sinninghe Damsté, J.S., Dickens, G.R.,
833 Huber, M., Reichart, G., Stein, R., Matthiessen, J., Lourens, L.J., Pedentchouk, N., Backman, J.,
834 Moran, K. and the Expedition 320 Scientists: Subtropical arctic ocean temperatures during the
835 Palaeocene/Eocene thermal maximum. *Nature* 441, 610–613, 2006.
- 836 Sluijs, A., Schouten, S., Donders, T. H., Schoon, P. L., Rohl, U., Reichart, G.-J., Sangiorgi, F., Kim, J.-H.,
837 Sinninghe Damsté, J. S., Brinkhuis, H.: Warm and wet conditions in the Arctic region during
838 Eocene Thermal Maximum 2, *Nature Geosci*, 2, 777-780, 2009.
- 839 Taylor, K. W. R., Willumsen, P. S., Hollis, C. J., Pancost, R. D.: South Pacific evidence for the long-term
840 climate impact of the Cretaceous/Paleogene boundary event, *Earth-Science Reviews*, 179, 287-302,
841 2018.
- 842 Taylor, K. W., Huber, M., Hollis, C. J., Hernandez-Sanchez, M. T., Pancost, R. D.: Re-evaluating modern
843 and Palaeogene GDGT distributions: Implications for SST reconstructions, *Global and Planetary
844 Change*, 108, 158-174, 2013.
- 845 Tierney, J. E.: GDGT Thermometry: Lipid Tools for Reconstructing Paleotemperatures. Retrieved from
846 https://www.geo.arizona.edu/~jesst/resources/TierneyPSP_GDGTs.pdf, 2012
- 847 Tierney, J. E., and Tingley, M. P.: A Bayesian, spatially-varying calibration model for the TEX₈₆ proxy.
848 *Geochimica et Cosmochimica Acta*, 127, 83-106, 2014.
- 849 Tierney, J. E., and Tingley, M. P.: A TEX₈₆ surface sediment database and extended Bayesian calibration,
850 *Scientific data*, 2, 150029, 2015.
- 851 Williams, C.K.I., and Rasmussen, C.E.: *Gaussian processes for machine learning*. MIT Press Cambridge,
852 MA, 2006.
- 853 Wuchter, C., Schouten, S., Coolen, M. J. L., and Sinninghe Damsté, J. S.: Temperature-dependent variation
854 in the distribution 30 of tetraether membrane lipids of marine Crenarchaeota: Implications for
855 TEX₈₆ paleothermometry, *Paleoceanography and Paleoclimatology*. doi:10.1029/2004PA001041,
856 2004.
- 857 Zhang, Y. G., and Liu, X.: Export Depth of the TEX₈₆ Signal. *Paleoceanography and Paleoclimatology*.
858 doi.org/10.1029/2018PA003337, 2018.
- 859 Zhang, Y. G., Pagani, M., Wang, Z.: Ring Index: A new strategy to evaluate the integrity of TEX₈₆
860 paleothermometry, *Paleoceanography*, 31, 220-232, 2016.
- 861 Zhang, Y. G., Zhang, C. L., Liu, X.-L., Li, L., Hinrichs, K.-U., Noakes, J. E.: Methane Index: a tetraether
862 archaeal lipid 15 biomarker indicator for detecting the instability of marine gas hydrates, *Earth and
863 Planetary Science Letters*, 307, 525- 534, 2011.
- 864 Zhang, Y.G., Pagani, M., Liu, Z.: A 12-million-year temperature history of the tropical Pacific
865 Ocean: *Science*, 343, 84-86, 2014.
- 866
- 867



Figure 1

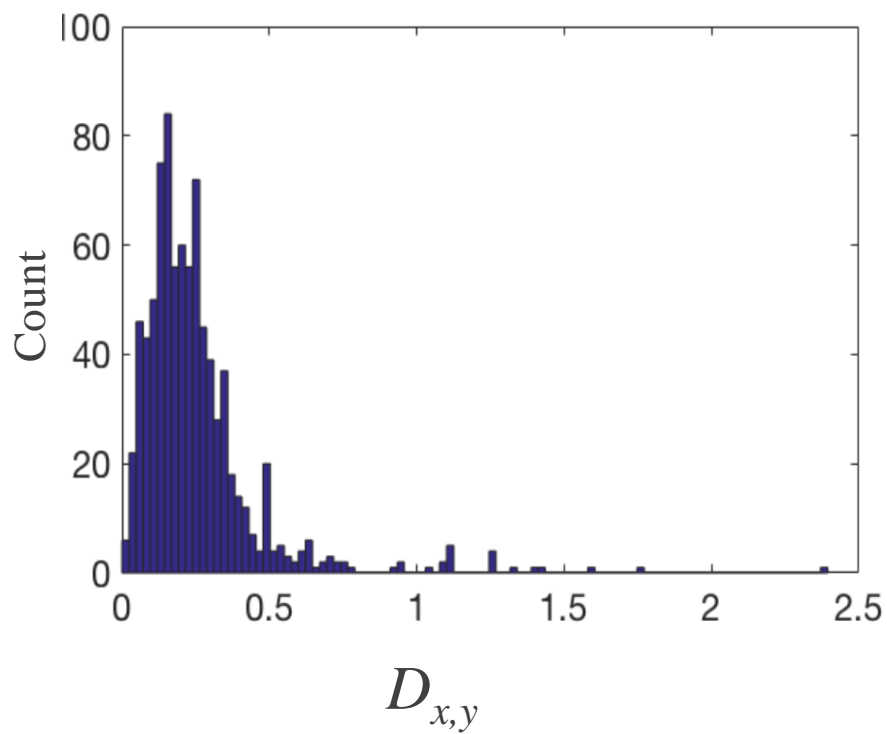




Figure 2

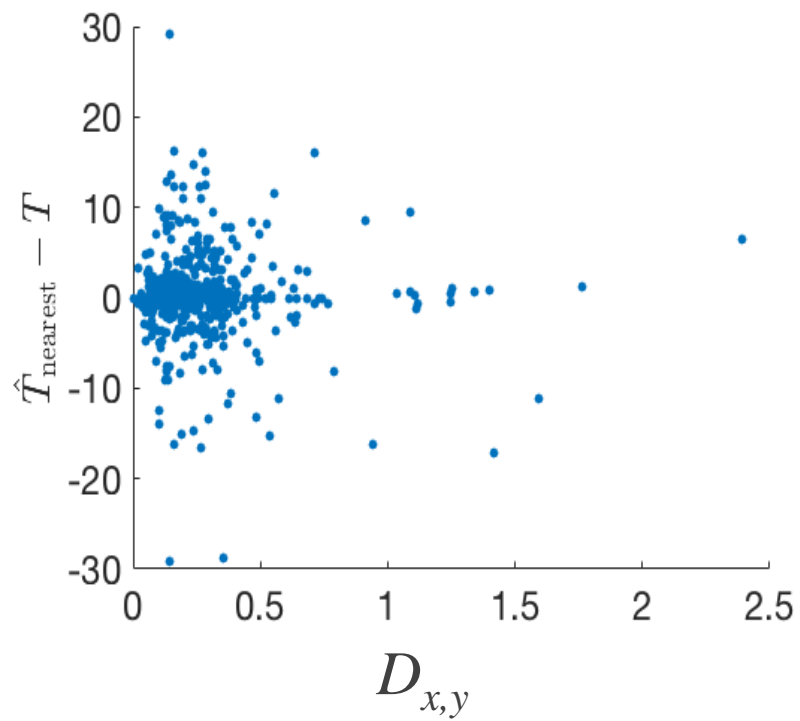




Figure 3

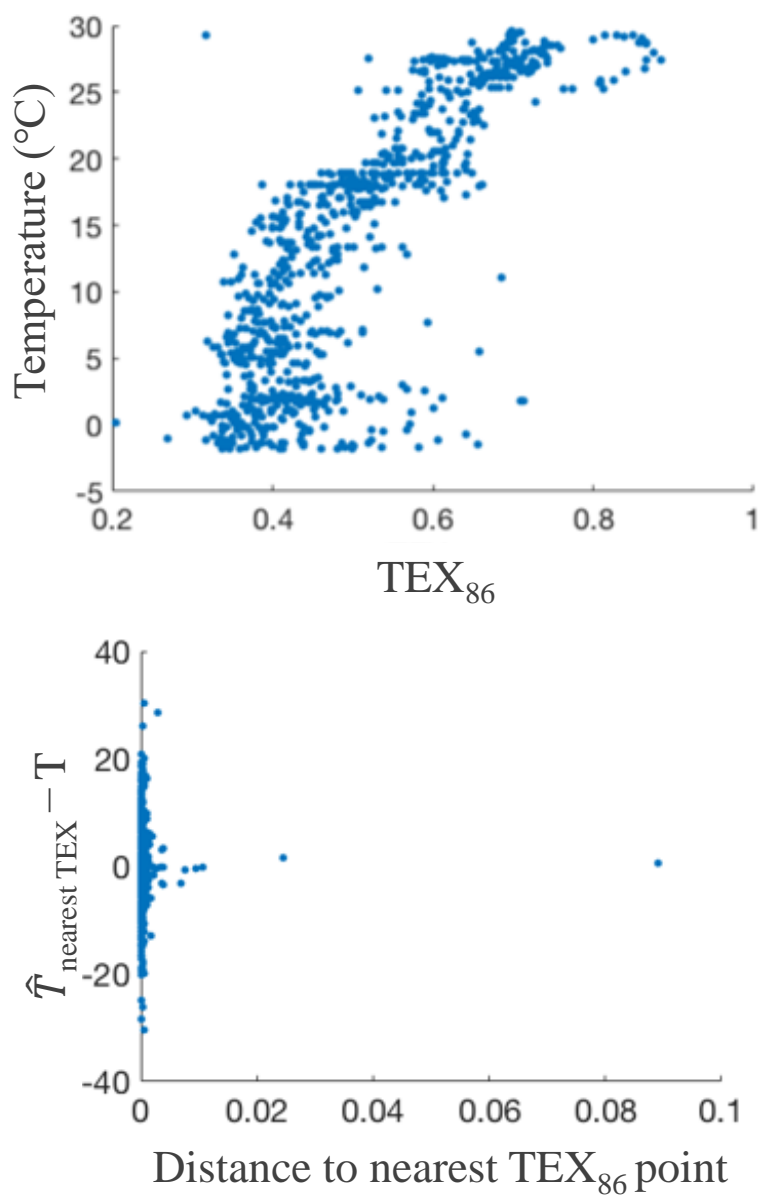




Figure 4

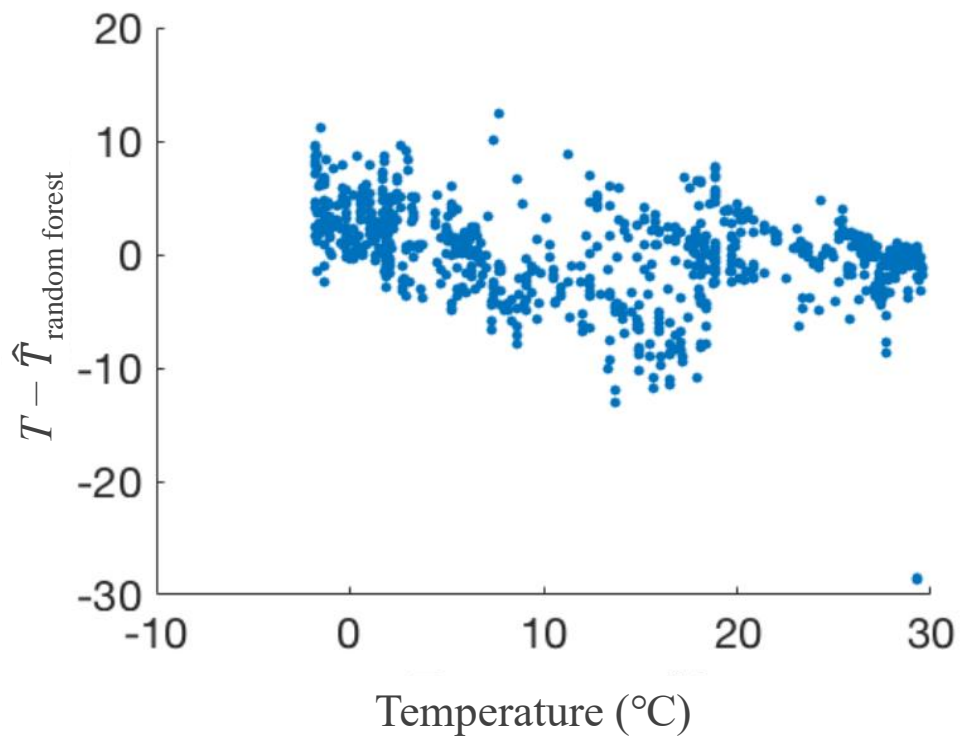




Figure 5

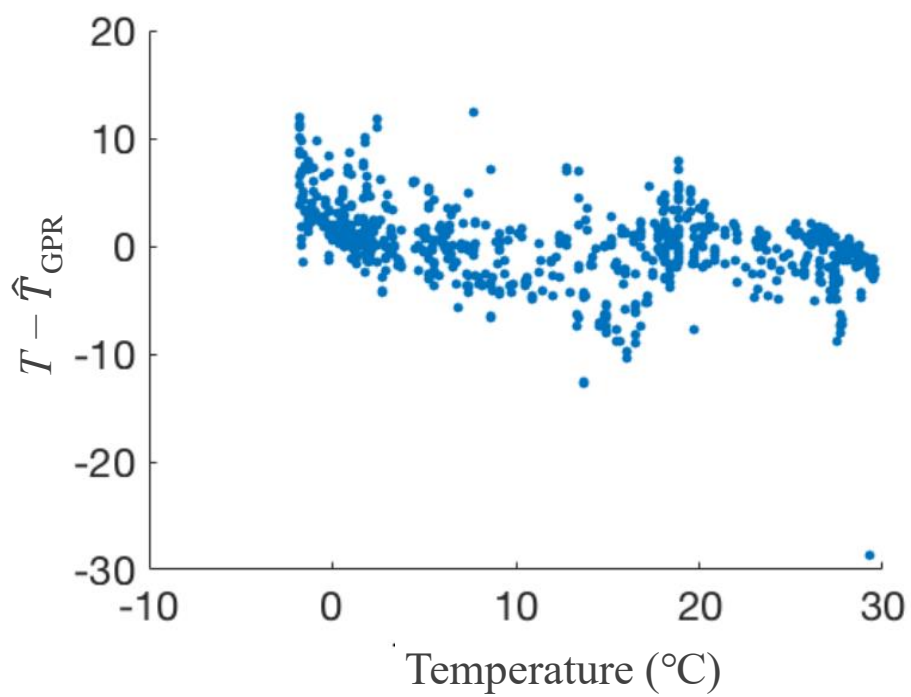




Figure 6

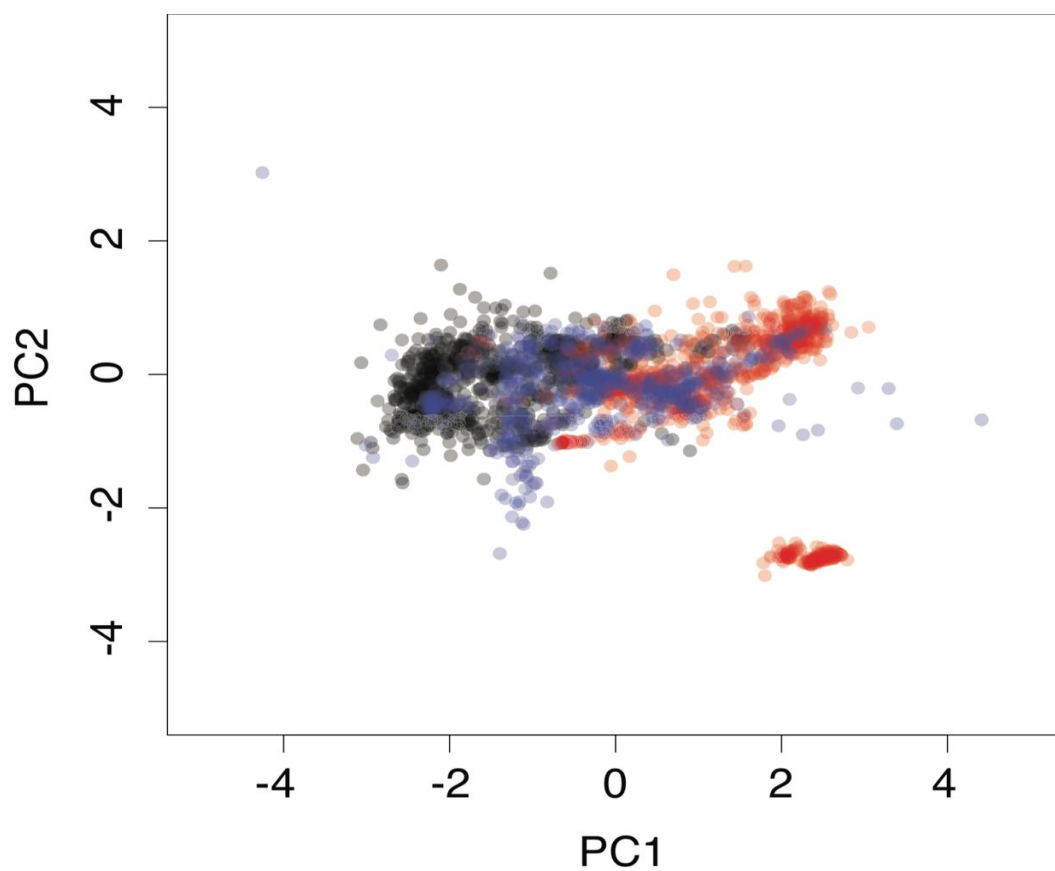




Figure 7

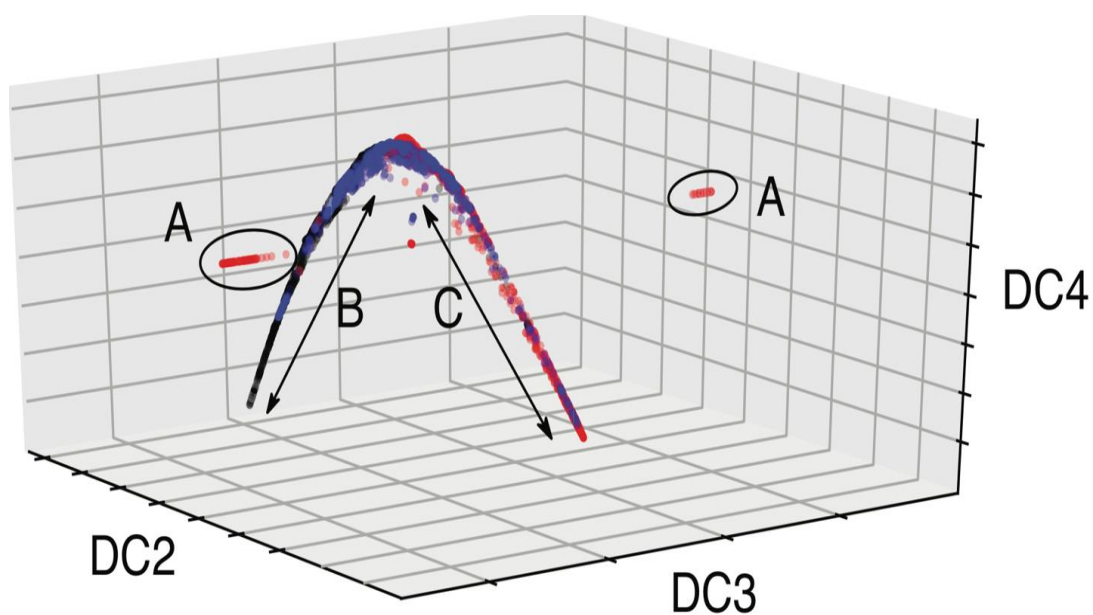




Figure 8

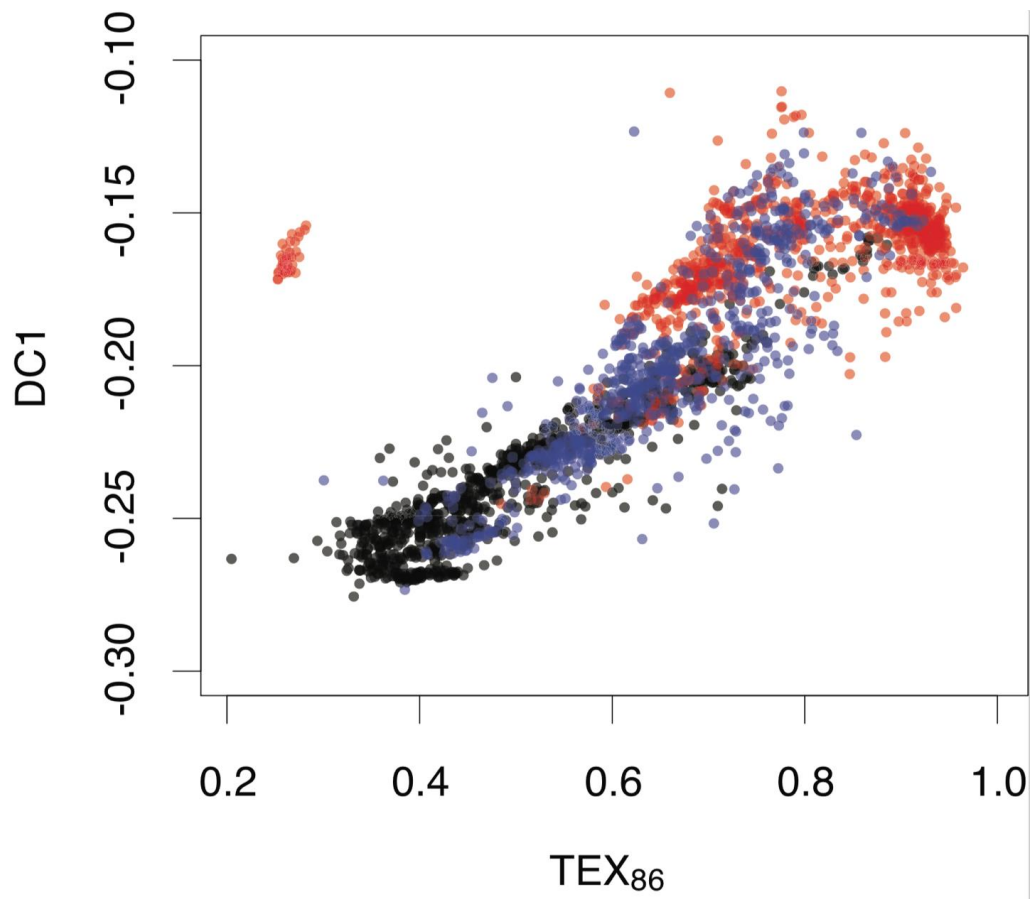




Figure 9

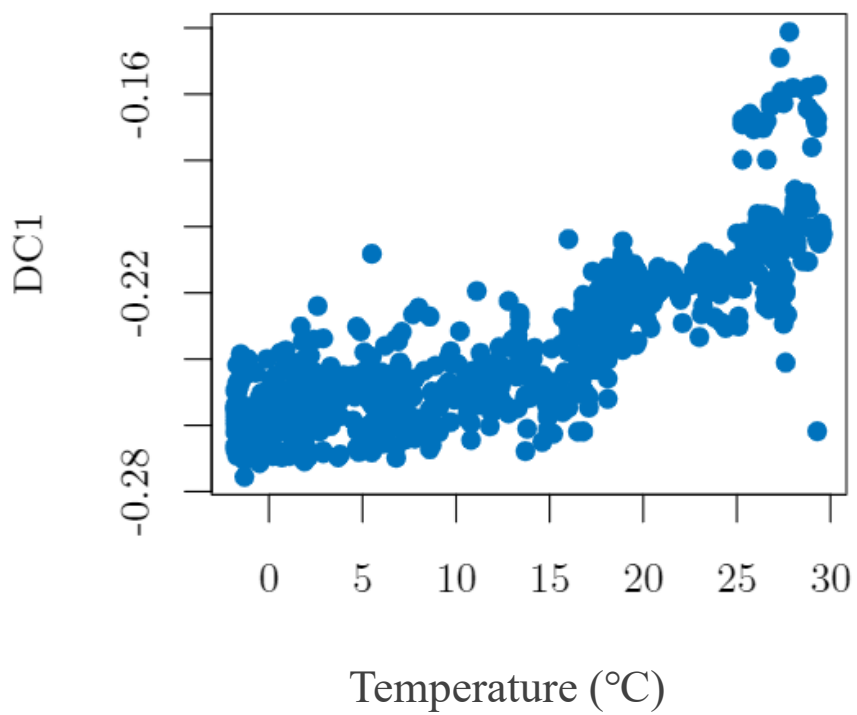




Figure 10

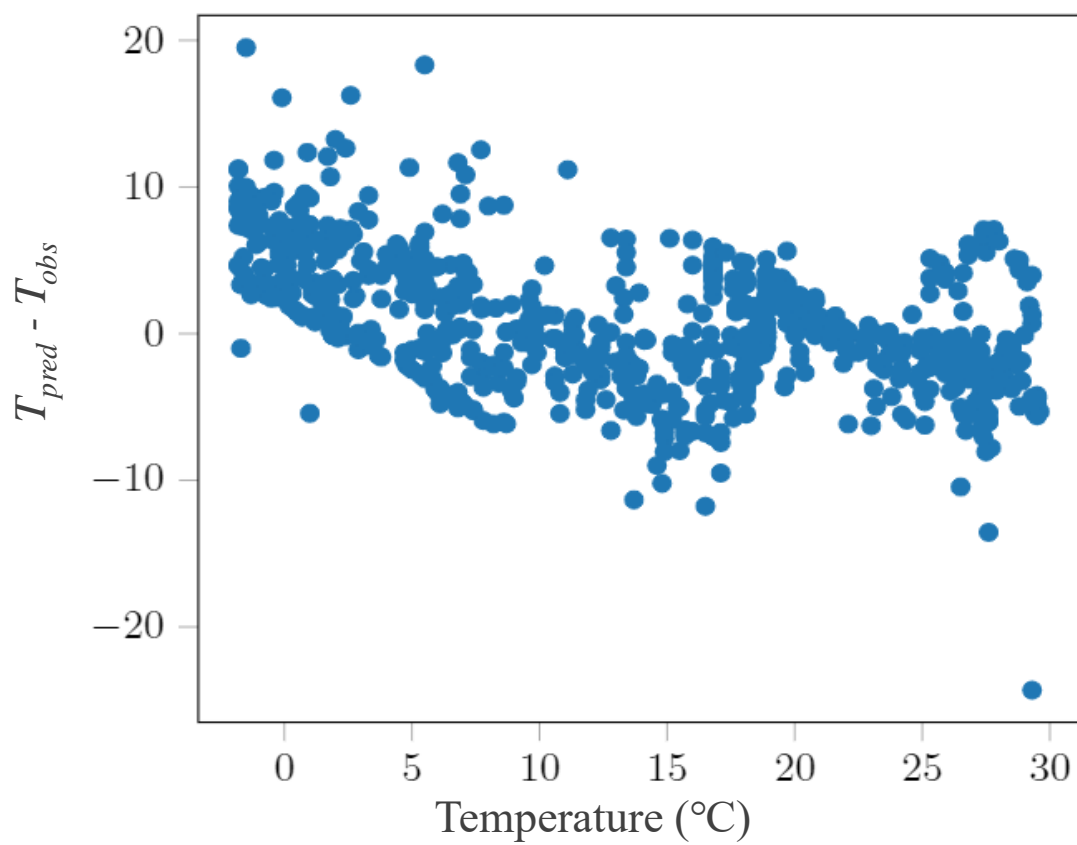




Figure 11

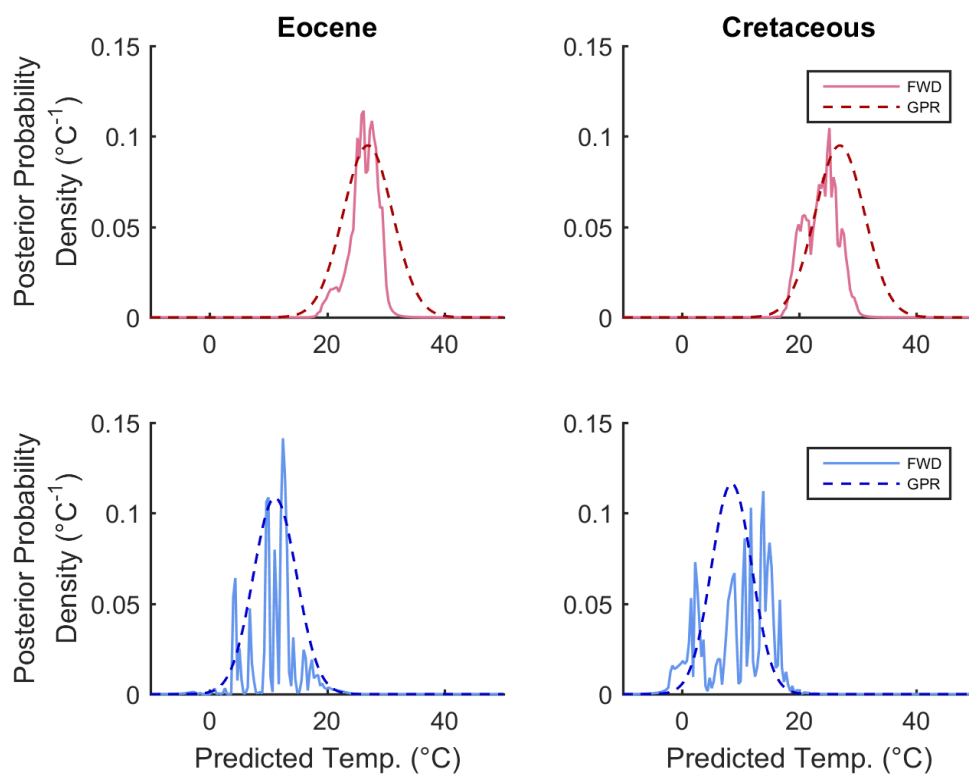




Figure 12

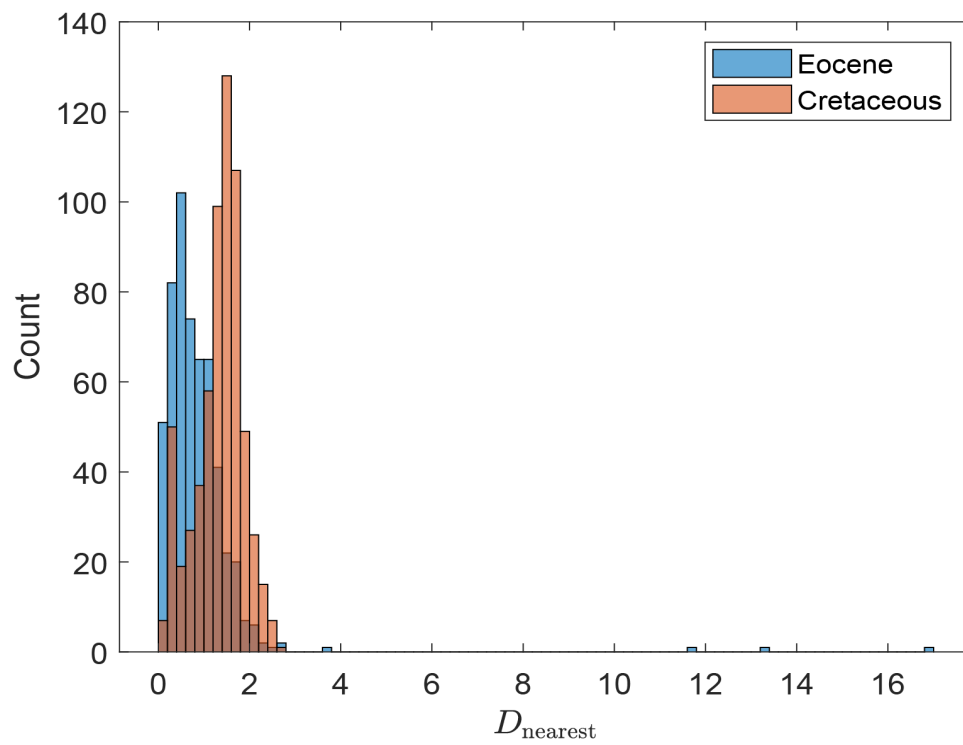




Figure 13

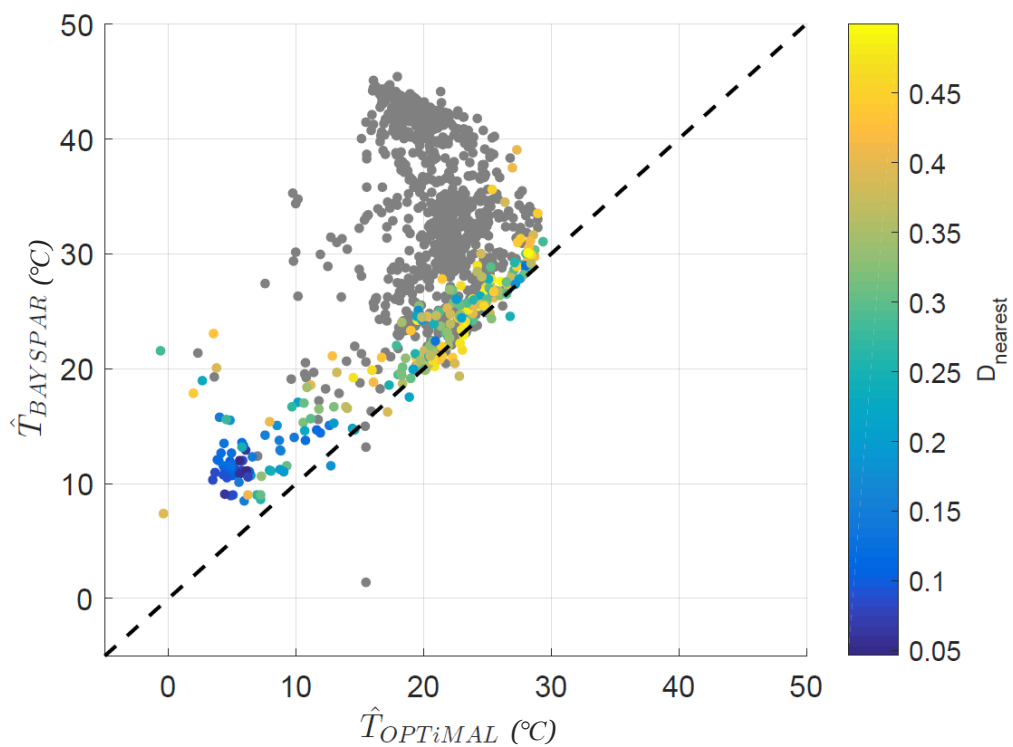




Figure 14

